Journal of Materials Science: Materials in Electronics
https://doi.org/10.1007/s10854-020-03086-3

Optical properties, microstructure, and multifractal analyses of ZnS thin films obtained by RF magnetron sputtering

Reza Shakoury[1] · Ali Arman[2] · Ştefan Ţălu[3] · Koushik Ghosh[4] · Sahar Rezaee[5] · Carlos Luna[6] · Fredrick Mwema[7,8] · Khalil Sherafat[2] · Maryam Salehi[2] · Mohsen Mardani[2]

Received: 2 December 2019 / Accepted: 10 February 2020
© Springer Science+Business Media, LLC, part of Springer Nature 2020

Abstract

The morphology, structure and optical properties of zinc sulfide (ZnS) thin films prepared through radio-frequency (RF) magnetron sputtering have been analyzed using atomic force microscopy (AFM), UV–Vis–NIR spectrophotometry, X-ray diffraction, and multifractal analyses. The X-ray diffraction patterns revealed that all ZnS thin films show a single peak at around 29.6°, which has been ascribed to the (111) planes of sphalerite phase, indicating that the growth direction of the films is the [111] direction. UV–Vis–NIR transmittance spectra were used to determine the refractive index of the samples, their thickness, and their band gap energy, showing the optical and semiconductor properties a clear dependence of the film thickness. Finally, ZnS thin films were characterized and analyzed by atomic force microscopy (AFM) measurements and multifractal analyses for a complex and precise interpretation of the 3-D surface microtexture characteristics. The multifractal examinations of the samples revealed a particular distribution at the nanometric level associated with multifractal surface characteristics. These experimental results are corroborated, presented, and discussed together with the essential stereometric parameters of the thin films. The combination of the different experimental information and the comprehensive stereometric and multifractal analyses provide new and deeper insight into the ZnS thin films that would be exploited to develop novel micro-topography models.

1 Introduction

Zinc sulfide (ZnS) is one of the metal chalcogenide that has attracted more interest of researchers in thin-film technology due to its high wide band gap (3.68 eV). It has significant applications in optics and electronics, solar systems, electroluminescence, optical sensors, laser devices, UV light-emitting diodes (LEDs), and many others. ZnS has excellent anti-reflective and coating characteristics due to its high refractive index value of 2.35 [1]. The growing demand in thin films for various applications, such as those mentioned above, inspires a continuous investigation about the deposition, performance, and applications of a wide range of thin-film materials, including ZnS.

Due to the attractive properties of the ZnS, several complex experimental and theoretical studies have been performed. These investigations show that ZnS thin films can be efficiently prepared by a variety of methods including chemical vapor deposition (CVD) [1], ionic layer adsorption and reaction techniques [2], chemical bath deposition [3, 4], chemical spray pyrolysis [5–7], electrochemical deposition

✉ Sahar Rezaee
Saharrezaee593@iauksh.ac.ir

[1] Department of Physics, Faculty of Science, Imam Khomeini International University, Qazvin, Iran

[2] Vacuum Technology Research Group, ACECR, Sharif University Branch, Tehran, Iran

[3] Development and Innovation Management (DMCDI), Technical University of Cluj-Napoca, The Directorate of Research, Constantin Daicoviciu St., No. 15, 400020 Cluj-Napoca, Cluj County, Romania

[4] Department of Pure and Applied Physics, Guru Ghasidas Vishwavidyalaya, Bilaspur, Chhattisgarh 495009, India

[5] Department of Physics, Kermanshah Branch, Islamic Azad University, Kermanshah, Iran

[6] Universidad Autónoma de Nuevo León (UANL), Facultad de Ciencias Físico Matemáticas (FCFM), Av. Universidad s/n, 66455 San Nicolás de Los Garza, Nuevo León, Mexico

[7] Mechanical Engineering Science, University of Johannesburg, Johannesburg, South Africa

[8] Department of Mechanical Engineering, Dedan Kimathi University of Technology, Nyeri, Kenya

Published online: 20 February 2020

[8], magnetron sputtering [9–11], pulsed laser deposition [12], sol–gel [13], and electron beam evaporation [14].

From the published works, it can be deduced that the conditions of the process greatly influence ZnS thin-film properties. For instance, the effect of spray rate on ZnS films prepared by chemical spray pyrolysis method on the structural and optical properties was reported by Al-Diabat et al. [15], in which XRD and UV–Vis absorption analyses techniques were used. Different studies have reported the effect of doping on the structural and optical properties of ZnS [8, 13, 16–19], and it is highlighted that the addition of impurities such as Cu, Gadolinium, Sn, Cd, Al, Co, and many others tunes the optical band gap and improves other properties of the ZnS thin films [16, 19, 20]. For instance, for improved performance as an emitter layer in photovoltaic devices, ZnS thin films must be doped with some metallic impurities such as Cr, Al, and transitional metals [20].

Sputtering is one of the most preferred techniques for the film fabrication due to its flexibility and production of high-quality thin films [21], which includes metallic, nonmetallic, and polymers specimens [22]. The critical issue during the sputtering process is to adjust the deposition parameters to obtain quality thin films. Various studies on the sputtering of ZnS have investigated the influence of some process parameters, and important advances have been achieved. For instance, the effect of the substrate type on ZnS thin films deposited on glass, indium titanium oxide (ITO), and corning glass through radio-frequency (RF) magnetron sputtered has been explored [23]. The complex structural characterizations revealed that thin films on corning glass exhibited better crystallinity, morphology, and electrical properties, indicating the significance of the substrate nature. Donne et al. [24] studied the effect of the sputtering power and deposition time on ZnS films prepared via RF magnetron sputtering at room temperature on lime glass substrates. This study based on AFM results reported that there exists an optimal RF power for the deposition of ZnS thin films with fewer surface defects and a lower roughness. Similar results concerning the effect of the sputtering power on the surface micromorphology of Al thin films prepared through RF magnetron sputtering has been reported [25, 26]. However, in other study, it was contrary revealed that ZnS deposited on ZnO substrate at 500 °C and in sulfur vapor exhibited a linear increase of crystallinity with a RF power from 40 to 120 W [27]. Similar trend for RF power on structure, morphology, and optical characteristics was reported by Kim et al. [28]. In another investigation, Chelvanathan et al. [29] investigated the influence of the substrate temperature of ZnS sputtered on soda-lime glass at a temperature range between 25 and 300 °C. The study revealed that the substrate temperature greatly influenced the grain size, crystallinity, and optical properties. More studies on the influence of other process parameters on properties of sputtered ZnS are available in the scientific literature [30, 31]. A conspicuous gap is obtained on the sputtering of ZnS adjusting the effect of argon gas flow rate and working pressure on the properties of the films. These parameters are responsible for the creation and sustenance of the plasma, which plays the major role of dislodging the target material and transporting it to the substrate surface. It means that these parameters influence both the sputtering yield and efficiency (as the mean free path is associated with the chamber pressure). It is expected in experimental studies that the choice of the right combination of these parameters contributes to enhancing their structure, morphology, and optical properties. Different studies applied fractal [32–34] and multifractal [35–37] geometry, stereometric analysis [38–41], and power spectral density (PSD) functions [42] for the analysis of the AFM data [43] to gain insight into the complex three-dimensional (3-D) surface morphology of thin films.

This article aims to report a detailed analysis of the morphology, structure, and optical properties of ZnS thin films prepared through RF magnetron sputtering with different working pressures and Ar gas flow rates. The combination of the different experimental information and the comprehensive stereometric and multifractal analyses provides a new and deeper insight of the physical properties of the ZnS thin films and their dependences on the deposition parameters.

2 Experimental section

In this work, ZnS thin films were prepared through RF magnetron sputtering. This method was chosen due to its flexibility and ability to deposit films under vacuum. The facility's vacuum system consists of two pumps: a mechanical rotary pump and a turbo pump. During the deposition process, the rotary pump is used to vacuum the system at a pressure of 0.05 Torr (low vacuum) beyond which the turbo pump is used to create a very high vacuum in the deposition chamber. The high vacuum is responsible for the creation of sustainable plasma and enhances the dislodgement of the target material resulting in impurity-free films. A disk of ZnS (purity of 99.9%) with a diameter of 100 mm was used as the target (cathode), while BK7 glasses were used as the substrates. Before deposition, these substrates were thoroughly cleaned in an ultrasonic bath with acetone to remove any embedded particles on their surfaces. They were rinsed in distilled water and dried in high pressure and hot air. The substrates were then mounted onto the substrate holder at a constant distance of 140 mm from the target surface. There was no heating of the substrates in this case, but because of the plasma and sputtering process, the temperature reached a maximum of 40 °C. The base pressure of the system was evacuated up to 2×10^{-6} Torr, and the working pressure was varied within the order of 10^{-3}. All of the samples have been

Table 1 Deposition parameters of the ZnS thin films

Samples	Argon gas flow rate (sccm)	Working pressure (mTorr)
S_1	20	4.4
S_2	40	6.2
S_3	60	8.1
S_4	80	9.7

prepared with a RF power of 70 W, and argon gas of 99.99% purity was used as the working gas. The argon gas flow rate was controlled by mass flow controllers. Pre-sputtering was conducted for 60 s under the deposition conditions with the target shutter closed. The film thickness and the rate of deposition were monitored by a crystal monitor. The deposition time for 1 h was used for all the samples. Table 1 describes the samples of ZnS prepared in this experiment. The effects of pressure and working gas flow rate on properties of the ZnS film were studied.

The crystalline structure of the films was characterized by X-ray diffraction with a 2θ angle in the range of 20–90 using Cu-Kα radiation in a step of 0.02. The crystal size of the samples was estimated calculating the size of the mean coherent diffraction domain, D, utilizing the Scherrer formula [44]:

$$D = \frac{0.90\lambda}{\beta\cos\theta} \tag{1}$$

where β is the full-width at half-maximum (FWHM) in radians and θ is the Bragg angle of the diffraction peak.

The transmission spectra were measured by spectrometer Rayleigh UV–visible 2601, over wavelengths from 400 to 1200 nm. Also, the scattering of samples was measured with an integrating sphere attachment. The thickness and the refractive index of samples were estimated from these spectra using the Swanepoel method [45, 46]. Therefore, the refractive index, $n = n(\lambda)$, was calculated using the following equation:

$$n = \sqrt{N + \sqrt{N^2 - s^2}} \tag{2}$$

where s is the substrate refractive index, and λ is the wavelength of the electromagnetic radiation, and $N = N(\lambda)$ is given by:

$$N(\lambda) = 2s\frac{T_M(\lambda) - T_m(\lambda)}{T_M(\lambda) \cdot T_m(\lambda)} + \frac{s^2 + 1}{2} \tag{3}$$

being $T_M = T_M(\lambda)$ and $T_m = T_m(\lambda)$, the transmittance maxima and minima of the interference fringes.

The film thickness was estimated from the interference fringes by means of the following formula [45, 46]:

$$t = \frac{\lambda_1\lambda_2}{2[\lambda_2 n(\lambda_1) - \lambda_1 n(\lambda_2)]} \tag{4}$$

where λ_1 and λ_2 are the wavelengths corresponding to two adjacent maxima or minima of the transmittance, respectively.

The direct transition band gap energy, E_G, of the different samples was estimated by means of the Tauc´s plot analysis utilizing the following formula [47]:

$$(\alpha h\nu)^2 = A\left(h\nu - E_G\right) \tag{5}$$

where α is the absorption coefficient, ν is the frequency of the photons, A is a constant, and h is the Plank´s constant.

Morphological properties of the films have been studied by Atomic Force Microscopy (AFM).

3 Results and discussion

Figure 1 shows the XRD patterns of the four studied samples. These diffractograms depict only one peak, corresponding to the crystalline growth direction of the films, which emerge with increasing intensity as the pressure and working gas flow rate increase. In this manner, this is more intense for sample S4, and it vanishes for sample S1. The only observed diffraction peak is located at 29.66°, 29.55°, and 29.58°, for samples S2, S3, and S4, respectively. These peak positions are shifted to the expected positions for the reflection ascribed to (002) and (101) of the wurtzite phase (JCPDS card No. 36–1450), which are at 28.48° and 30.53°, respectively, and the reflection ascribed to the (111) reflection of

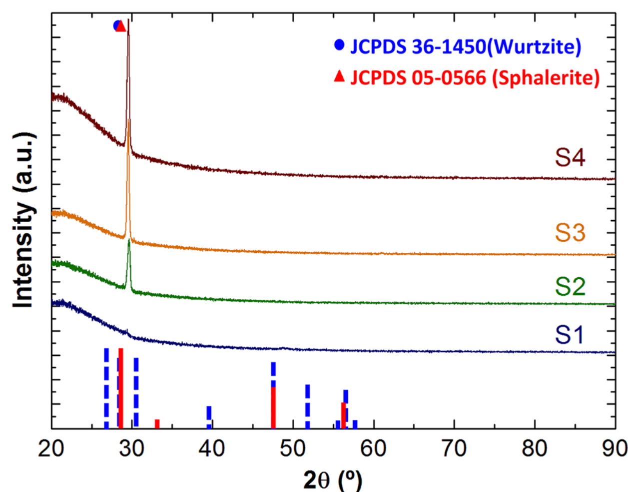

Fig. 1 XRD patterns of the four studied samples. The reference patterns of the wurtzite (JCPDS card no. 36–1450) and sphalerite (JCPDS card no. 05–0566) are represented with blue and red bars, respectively (Color figure online)

the sphalerite phase (JCPDS card No. 05-0566), which is at 28.58°. The crystal size calculated from the diffraction peak using the Scherrer formula [44] is 20, 30, and 24 nm for samples S2, S3, and S4, respectively.

The AFM micrographs of samples were processed with MountainsMap® Premium software ver. 8.0 [48]. Figure 2 shows the surface morphology of samples with specific nanopatterns.

The interface width profiles obtained from the AFM micrographs are shown in Fig. 3 (in distinct color for every sample), representing the root mean square height (RMS) as a function of length. This dependence is an important part of measuring the depth profile of a thin-film structure. The lowest value of RMS was found for sample S1 (3.1 ± 0.38 nm), while the highest value of RMS was found for sample S4 (16.7 ± 3.8 nm); samples S3 and S4 have similar medium RMS values (according Table 3).

The representation of the surface texture directions of analyzed samples using Cartesian graphs is shown in Fig. 4, and the corresponding values are given in Table 2.

It can be seen that the isotropy parameter has the highest value for sample S3 (57.33%), while the lowest value was found for sample S4 (52.88%). The highest value of the first

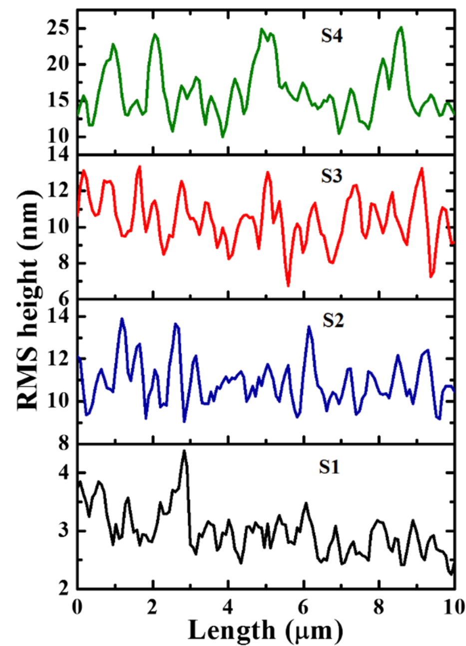

Fig. 3 Interface width profiles of AFM micrographs of samples: (a) S1, (b) S2, (c) S3, (d) S4

Fig. 2 3-D AFM micrographs of ZnS thin films of samples: (**a**) S1, (**b**) S2, (**c**) S3, (**d**) S4

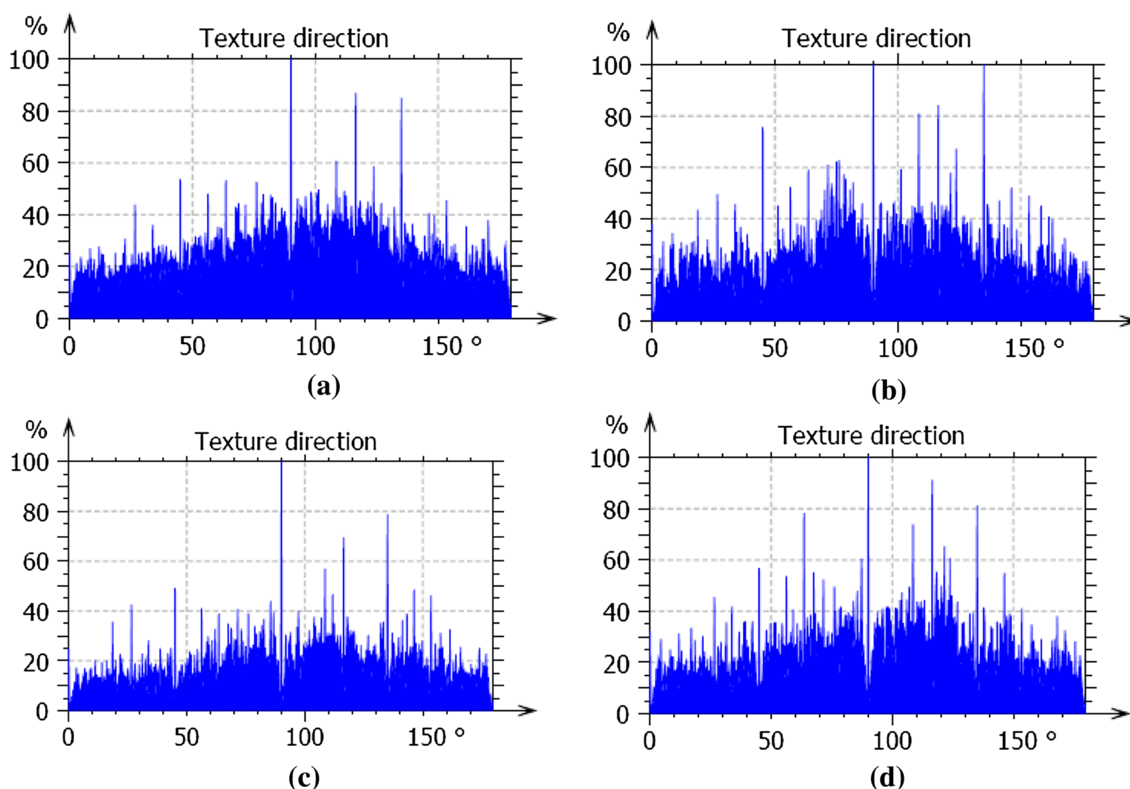

Fig. 4 The representation of surface texture directions of samples using Cartesian graphs for **a** S1, **b** S2, **c** S3, **d** S4

Table 2 The surface texture directions of analyzed samples using Cartesian graphs

Parameters	S1	S2	S3	S4
Isotropy (%)	53.76	54.22	57.33	52.88
First direction (°)	89.98	135.0	90.02	90.00
Second direction (°)	116.5	90.01	135.0	116.5
Third direction (°)	135.0	116.4	116.5	135.0

direction parameter is observed in the sample S2 (135.0°), whereas the lowest values of this parameter are reached for all other samples (S1, S3, and S4). The highest value of second direction parameter appears in the sample S3 (135.0°), while the lowest value is found for the sample S2 (90.01°); the other samples have the same values (116.5°). The highest value of the third direction parameter is observed in the samples S1 and S4 (135.0°), whereas the lowest values of this parameter are reached for the other samples S2 and S3 (116.5°).

The surface skewness (Ssk) parameter of all samples is positive (Ssk > 0). It indicates the dominance of peaks on their surface, and the highest value is associated with the sample S4 (1.5 ± 0.5), while the lowest value was found for the sample S1 (0.3 ± 0.4). For samples S1, S3, and S4, the surface kurtosis (Sku) parameter is positive (0 < Ssk < 3, for bumpy surfaces), while for S2 , the surface kurtosis (Sku) parameter is negative. The Sku parameter qualifies the flatness of the height distribution. The representation of cube count versus size plots to calculate the monofractal dimension (represented as log [N(ε)] versus log[1/ε]) is shown in Fig. 5, and the corresponding values are given in Table 3. As can be seen, the highest and lowest monofractal dimension for samples belong to S2 (2.56 ± 0.05) and S4 (2.43 ± 0.04), respectively, whereas intermediate values belong to samples S3 (2.53 ± 0.06) and S1 (2.45 ± 0.03), respectively.

Multifractal analysis, as a precise mathematical method for studying the local similarity of the surface topography, is a generalization of the fractal geometry approach and is effective if a single fractal measure cannot describe the local characteristics of thin-film morphology. In order to minimize the influence of the external values $h(x, y)$ on the multifractal characteristics, we applied the multifractal detrended fluctuation analysis (MFDFA) method to calculate the generalized Hurst exponents, mass exponents, and the multifractal singularity spectrum, $f(\alpha)$ [35–37]. These functions provide useful information to study structural details on the surface of samples. In this study, momentum values q are set from −10 to +10. The generalized Hurst exponents (H_q) have values in the range between 2.65 and 3.33, see

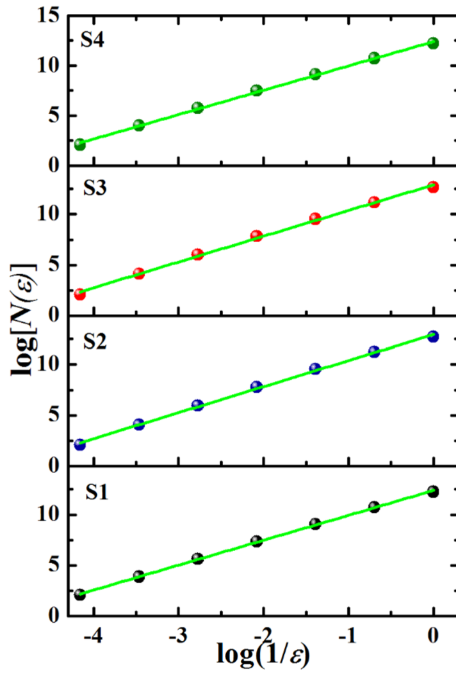

Fig. 5 Cube count versus size plots to calculate the monofractal dimension for (a) S1, (b) S2, (c) S3, (d) S4

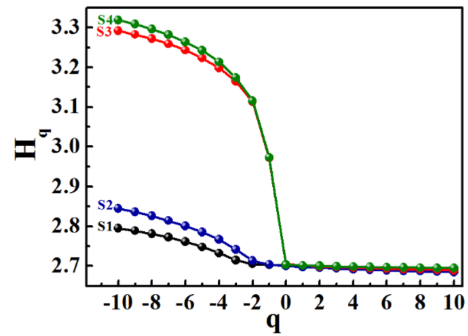

Fig. 6 The generalized Hurst exponents (H_q) versus statistical moments plot (q) for (a) S1, (b) S2, (c) S3, (d) S4

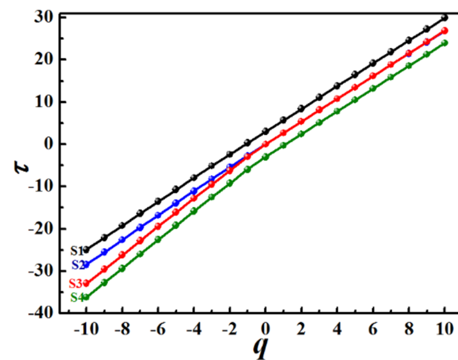

Fig. 7 Mass exponents (τ) as a function of statistical moments q for (a) S1, (b) S2, (c) S3, (d) S4

Fig. 6. It can be seen that the highest values are associated with the samples S4 and S3, while the lowest values are found for the samples S2 and S1, in the range of $-10 < q < 0$. The generalized Hurst exponents have values in the range of $2.65 < H_q < 2.7$ for $0 < q < 10$.

The non-uniformity of the nano-irregularities is also correlated with the mass exponents τ represented as a function of statistical moments q (Fig. 7). In this case, it can be seen that the values of mass exponents increase from sample S4 towards samples S3, S2, and S1, in the range of $-37 < \tau < 30$ for $-10 < q < 10$.

The multifractal singularity spectrum $f(\alpha)$ versus α was calculated for all samples. It is graphically represented in Fig. 8, where the $f(\alpha)$ spectrum was computed in the range $-10 \le q \le 10$. As can be seen in Fig. 8, the curve $f(\alpha)$ versus α is a non-linear asymmetric curve that has two arms and a width Δα. The left shoulder of the multifractal singularity spectrum $f(\alpha)$ is much shorter than the right one. On the other hand, the right shoulder of the multifractal singularity spectrum $f(\alpha)$ for sample S4 is much longer than those of the other samples. The surface of S4 sample exhibits the most irregular topography (Δα = 0.72, value bigger than the values of the other samples). On the other hand, the more regular film surface was found for the surface of sample S1 (Δα = 0.17) (Table 4). On the other hand, the left arm of the multifractal spectrum corresponds to strongly irregular areas, defined by a high dimension value, while the right arm of $f(\alpha)$ is associated with flat zones. Δα is the multifractal width spectrum, $\Delta\alpha = \alpha_{max} - \alpha_{min}$. Δf is the

Table 3 Conventional surface roughness parameters and monofractal dimension computed from the ZnS surface micrographs deposited at different deposition conditions

Sample name	Interface width (nm)	Root mean square height (nm)	Skewness (–)	Kurtosis (–)	Monofractal dimension (–)	Hurst exponent
S1	3.0 ± 0.4	3.1 ± 0.38	0.3 ± 0.4	0.2 ± 1.5	2.45 ± 0.03	0.55 ± 0.03
S2	11.0 ± 1.0	11.1 ± 0.9	0.6 ± 0.2	-0.4 ± 0.6	2.56 ± 0.05	0.46 ± 0.05
S3	10.0 ± 1.0	10.5 ± 0.9	1.2 ± 0.3	1.2 ± 1.3	2.53 ± 0.06	0.47 ± 0.06
S4	17.0 ± 4.0	16.7 ± 3.8	1.5 ± 0.5	3.0 ± 2.0	2.43 ± 0.04	0.57 ± 0.04

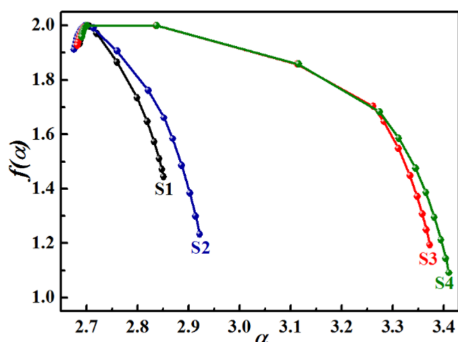

Fig. 8 The multifractal singularity spectrum, $f(\alpha)$, of samples: (a) S1, (b) S2, (c) S3, (d) S4

difference of the spectrum arms heights $\Delta f = f(\alpha_{max}) - f(\alpha_{min})$. As can be seen from Table 4, $\Delta\alpha$ and Δf have positive values.

The surface of sample S4 has the higher spectrum arms' heights difference Δf ($\Delta f = 0.87$). On the other hand, the lowest spectrum arms' heights difference Δf ($\Delta f = 0.49$) is found for the surface of sample S1 (Table 4).

Determined mass exponents and the multifractal singularity spectrum $f(\alpha)$ functions indicate multifractal properties of ZnS thin films, which are influenced by changes in the self-similarity and scaling properties of observed surface features.

Figure 9 shows the averaged power spectrum density (PSD) of all samples. It can be seen that there is the same wavelength of 1.770 µm for all samples, considering the same zoom factor × 4. In addition, the sample S4 has the lowest value of amplitude (0.02587 nm); the middle values belong to sample S1 (0.1134 nm) and sample S2 (0.1457 nm), while the highest value belongs to sample S3 (0.1883 nm). The samples S2, S3, and S4 have the same dominant wavelength at 0.1133 µm, while the sample S1 has the dominant wavelength at 0.2265 µm. The sample S1 has the lowest maximum amplitude (2.668 nm), the middle values belong to samples S3 (8.728 nm) and S2 (9.728 nm), while the highest value belongs to sample S4 (12.08 nm).

Figure 10 depicts the slices of samples.

The conventional surface roughness parameters, monofractal dimension, and the Hurst exponents are computed in Table 3, and the multifractal parameters of the ZnS surfaces deposited at different deposition conditions are given in Table 4.

Figure 11 depicts the transmittance spectra of the four samples. These spectra show interference fringes that are shifted as the working pressure and the gas flow rate are increased. The average transmittance at wavelengths between 450 and 1200 nm is around 77.7% for all samples.

Figure 12 shows the dependence of the refractive index on the radiation wavelength calculated using the Swanepoel method [45, 46]. It is observed that $n(\lambda)$ decreases as the working pressure and gas flow rate increase during the film deposition. The film thickness calculated using Eq. (4) is presented in Table 5.

The absorption spectra of the ZnS thin films are shown in Fig. 13. These data are represented in Tauc plots in Fig. 14, and the obtained band gap energy and the thickness of all ZnS thin films are presented in Table 5. It is observed that the values of band gap increased from sample S1 towards samples S2, S3, and S4, in the range from 2.95 to 2.99, while the film thickness decreased from sample S1 towards samples S2, S3, and S4, in the range of 1.38 to 0.96. Thus, E_G increases as the film thickness is decreased, probably due to confinement and surface effects [47].

4 Conclusions

The optical, semiconductor, and 3-D surface micromorphology of the ZnS thin films deposited on glass substrates by RF magnetron sputtering with different working pressures and Ar gas flow rates were determined using appropriate instruments and test methods. The 3-D surface microtexture of all samples in amplitude, spatial distribution, and pattern of surface characteristics highlighted multifractal characteristics quantified by the multifractal detrended fluctuation analysis (MFDFA) method. It was found that the most irregular topography was found for sample S4 ($\Delta\alpha = 0.72$), while the most regular topography was found for sample S1 ($\Delta\alpha = 0.17$). The most regular surface was found for sample S1 (RMS = 3.1 ± 0.38 nm), while the most irregular was the surface S4 (RMS = 16.7 ± 3.8 nm). Multifractal approach in correlation with the surface statistical parameters is a useful tool for quantifying the 3-D surface morphology of ZnS thin films.

The refractive index decreases as the pressure and working gas flow rate increase, and the film thickness decreases, whereas the band gap energy has the contrary tendency. The

Table 4 Multifractal parameters of ZnS thin-film surface micrographs computed using multifractal detrended fluctuation analysis (MFDFA) method

Sample	$f(\alpha)_{max}$	$f(\alpha)_{min}$	Δf	α_{max}	α_{min}	$\Delta\alpha$
S1	1.93	1.44	0.49	2.85	2.68	0.17
S2	1.91	1.23	0.68	2.92	2.67	0.25
S3	1.93	1.19	0.74	3.37	2.68	0.69
S4	1.96	1.09	0.87	3.41	2.69	0.72

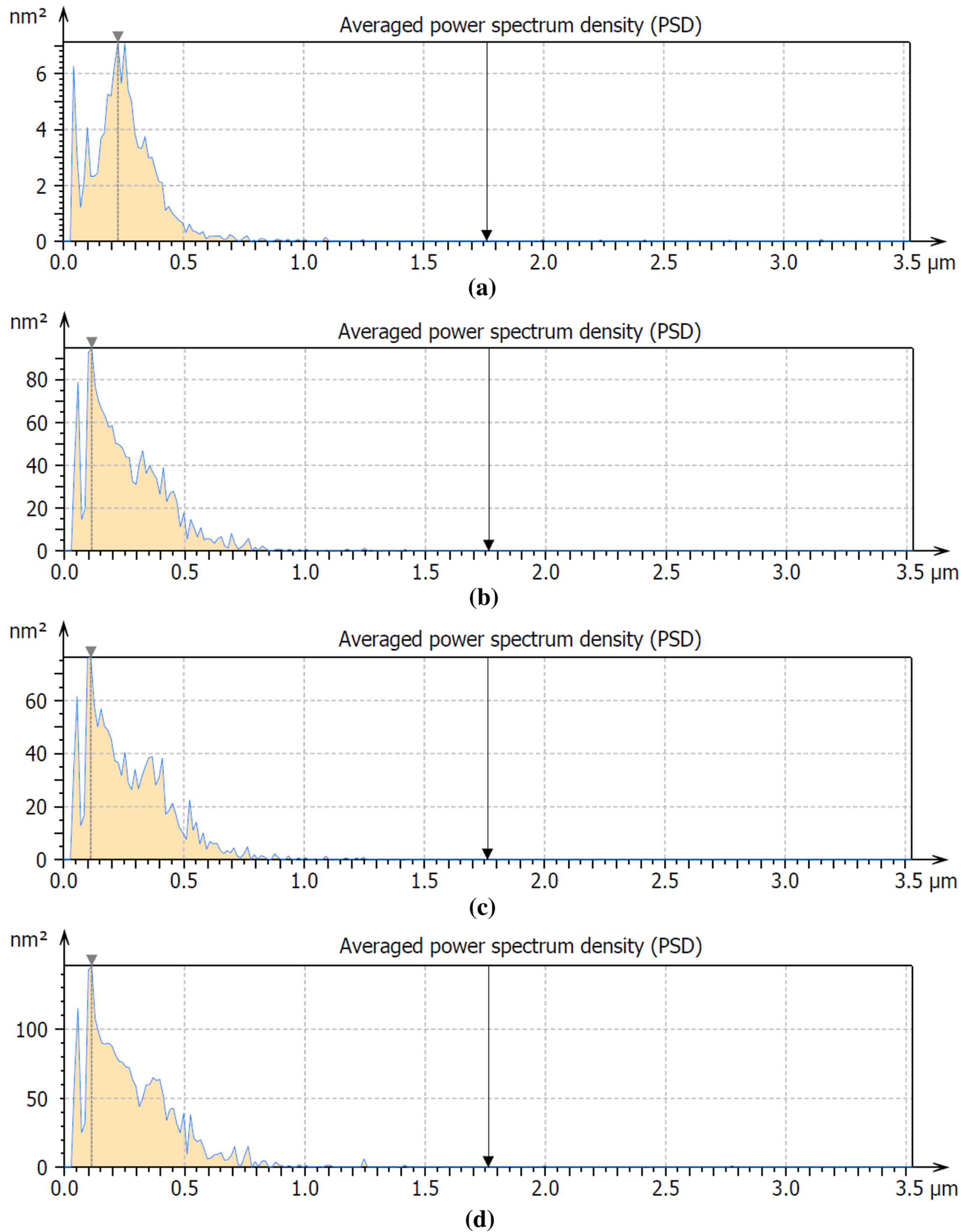

Fig. 9 The averaged power spectral density (surface) for the samples: **a** S1, **b** S2, **c** S3, **d** S4

optical analyses combined with the stereometric and multifractal analyses provided a deeper analysis that can serve as a foundation for the development of novel micro-topography models of ZnS thin films deposited on glass substrates by RF magnetron sputtering.

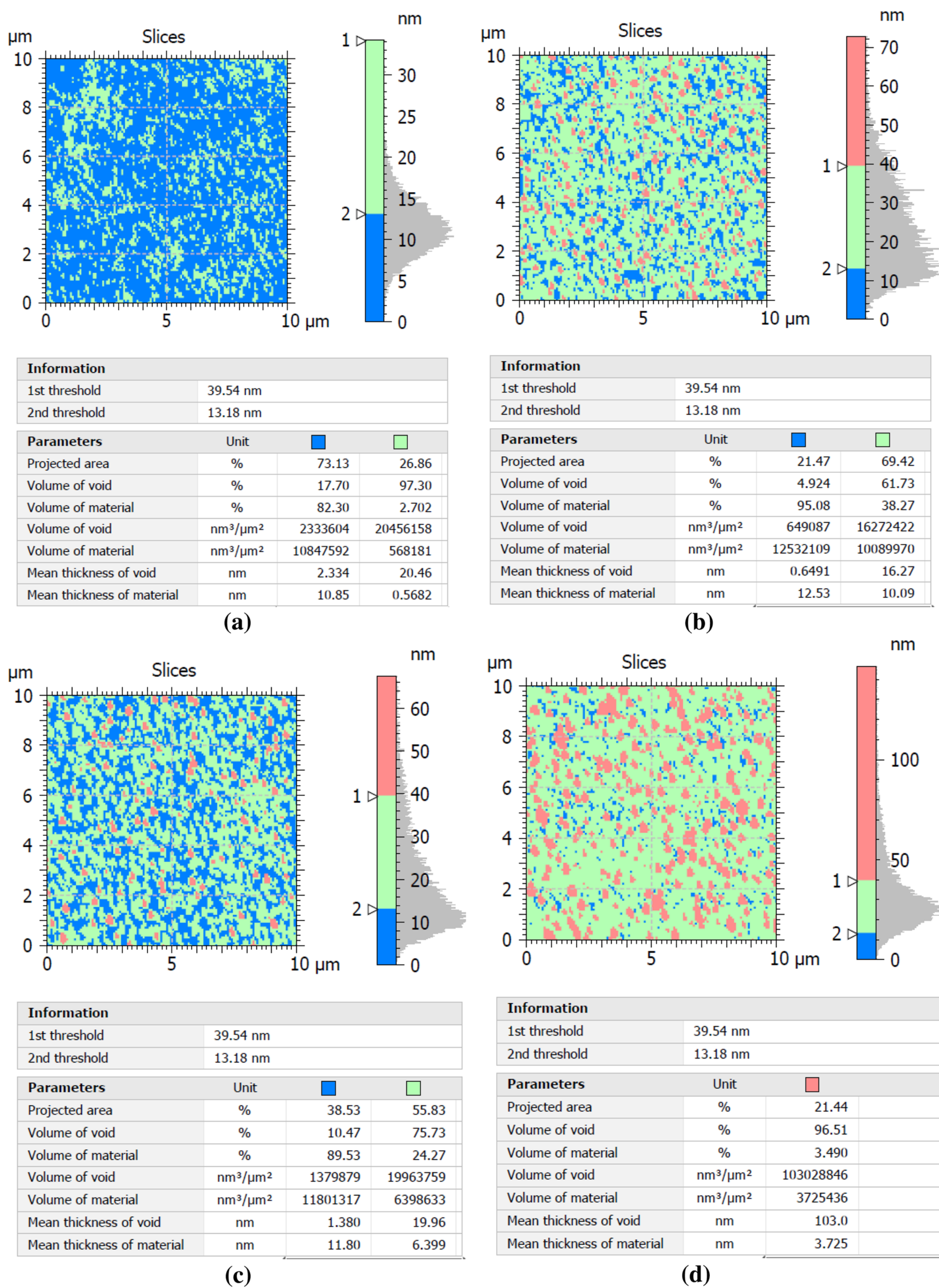

(a)

Information	
1st threshold	39.54 nm
2nd threshold	13.18 nm

Parameters	Unit	Blue	Green
Projected area	%	73.13	26.86
Volume of void	%	17.70	97.30
Volume of material	%	82.30	2.702
Volume of void	nm³/µm²	2333604	20456158
Volume of material	nm³/µm²	10847592	568181
Mean thickness of void	nm	2.334	20.46
Mean thickness of material	nm	10.85	0.5682

(b)

Information	
1st threshold	39.54 nm
2nd threshold	13.18 nm

Parameters	Unit	Blue	Green
Projected area	%	21.47	69.42
Volume of void	%	4.924	61.73
Volume of material	%	95.08	38.27
Volume of void	nm³/µm²	649087	16272422
Volume of material	nm³/µm²	12532109	10089970
Mean thickness of void	nm	0.6491	16.27
Mean thickness of material	nm	12.53	10.09

(c)

Information	
1st threshold	39.54 nm
2nd threshold	13.18 nm

Parameters	Unit	Blue	Green
Projected area	%	38.53	55.83
Volume of void	%	10.47	75.73
Volume of material	%	89.53	24.27
Volume of void	nm³/µm²	1379879	19963759
Volume of material	nm³/µm²	11801317	6398633
Mean thickness of void	nm	1.380	19.96
Mean thickness of material	nm	11.80	6.399

(d)

Information	
1st threshold	39.54 nm
2nd threshold	13.18 nm

Parameters	Unit	Red
Projected area	%	21.44
Volume of void	%	96.51
Volume of material	%	3.490
Volume of void	nm³/µm²	103028846
Volume of material	nm³/µm²	3725436
Mean thickness of void	nm	103.0
Mean thickness of material	nm	3.725

Fig. 10 The slices for the samples: **a** S1, **b** S2, **c** S3, **d** S4

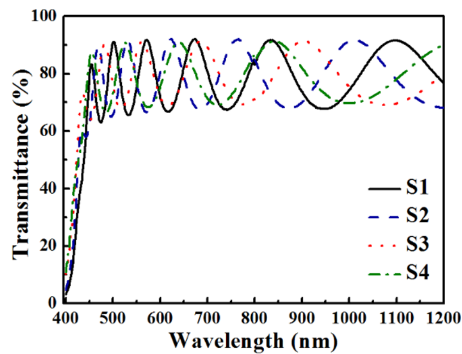

Fig. 11 UV–Vis–NIR transmittance spectra of ZnS thin films deposited at different deposition conditions for samples: (a) S1, (b) S2, (c) S3, (d) S4

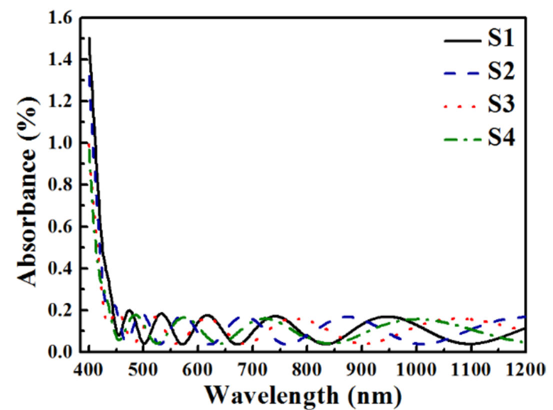

Fig. 13 Absorption spectra of ZnS thin films for (a) S1, (b) S2, (c) S3, (d) S4

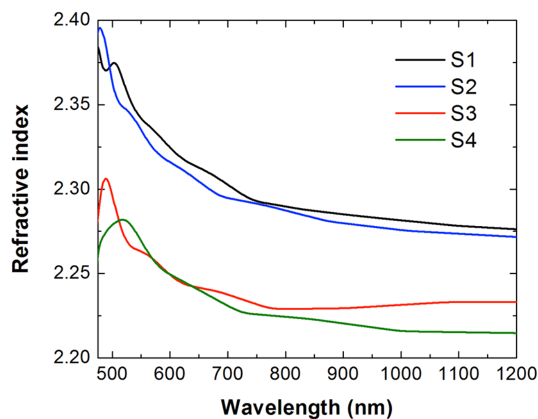

Fig. 12 Refractive index as a function of the radiation wavelength calculated using the Swanepoel method [45, 46]

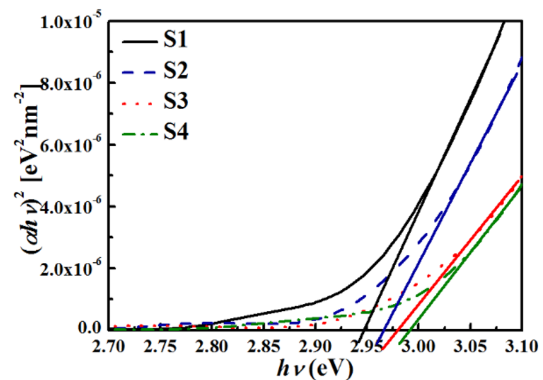

Fig. 14 Tauc plot of ZnS thin films for (a) S1, (b) S2, (c) S3, (d) S4

Table 5 Optical band gap and thickness calculated from the transmittance spectra of ZnS thin films deposited at different deposition conditions

Sample name	Band gap energy (eV)	Film thickness (nm)
S1	2.95	810 ± 70
S2	2.97	696 ± 25
S3	2.98	680 ± 45
S4	2.99	596 ± 5

Compliance with ethical standards

Conflict of interest Neither author has a financial or proprietary interest in any material or method mentioned. The authors declare that they have no competing interests.

References

1. A.M. Palve, Deposition of zinc sulfide thin films from Zinc(II) thiosemicarbazones as single molecular precursors using aerosol assisted chemical vapor deposition technique. Front. Mater. **6**, 46 (2019). https://doi.org/10.3389/fmats.2019.00046
2. V.K. Ashith, K. Gowrish Rao, Structural and optical properties of ZnS thin films by SILAR technique obtained by acetate precursor. IOP Conf. Ser. Mater. Sci. Eng. **360**(1), 012058 (2018). https://doi.org/10.1088/1757-899X/360/1/012058
3. P.E. Agbo, P.A. Nwofe, L.O. Odo, Analysis on energy bandgap of zinc sulphide (ZnS) thin films grown by solution growth technique. Chalcogenide Lett. **14**(8), 357–363 (2017)
4. G. Arandhara, J. Bora, P.K. Saikia, Effect of pH on the crystallite size, elastic properties and morphology of nanostructured ZnS thin films prepared by chemical bath deposition technique. Chem. Phys. Mater. (2020). https://doi.org/10.1016/j.matchemphys.2019.122277

5. P.O. Offor, B.A. Okorie, C.D. Lokhande, P.S. Patil, F.I. Ezema, A.D. Omah, V.S. Aigbodion, B.A. Ezekoye, I.C. Ezema, The properties of spray-deposited zinc sulfide thin films using trisodium citrate complexant. Int. J. Adv. Manuf. Technol. **95**(5–8), 1849–1857 (2018). https://doi.org/10.1007/s00170-017-1326-6
6. A. Jesu Jebathew, M. Karunakaran, K.D.A. Kumar, S. Valanarasu, V. Ganesh, S. Mohd Shkir, A.K. AlFaify, Effect of novel Nd3+ doping on physical properties of nebulizer spray pyrolysis fabricated ZnS thin films for optoelectronic technology. Phys B **572**, 109–116 (2019). https://doi.org/10.1016/j.physb.2019.07.042
7. K. Ben Bacha, N. Bitri, H. Bouzouita, Effect of annealing parameters on structural and morphological properties of sprayed ZnS thin films. Optik (Stuttg) **127**(5), 3100–3104 (2016). https://doi.org/10.1016/j.ijleo.2015.12.083
8. A. Azmand, H. Kafashan, Al-doped ZnS thin films: physical and electrochemical characterizations. J. Alloys Compd. **779**, 301–313 (2019). https://doi.org/10.1016/j.jallcom.2018.11.268
9. O. Toma, L. Ion, S. Iftimie, V.A. Antohe, A. Radu, A.M. Raduta, D. Manica, S. Antohe, Physical properties of rf-sputtered ZnS and ZnSe thin films used for double-heterojunction ZnS/ZnSe/CdTe photovoltaic structures. Appl. Surf. Sci. **478**, 831–839 (2019). https://doi.org/10.1016/j.apsusc.2019.02.032
10. S.R. Chalana, V.S. Kavitha, R. Reshmi Krishnan, V.P. Mahadevan Pillai, Tailoring the visible emissions in ZnS: Mn films for white light generation. J. Alloys Compd. **771**, 721–735 (2019). https://doi.org/10.1016/j.jallcom.2018.08.275
11. S. Chen, R. Yu, L. Song, R. Zhang, X. Cao, B. Wang, P. Zhang, Effect of low temperature vulcanization time on the structure and optical properties of ZnS thin films. Appl. Surf. Sci. **498**, 143876 (2019). https://doi.org/10.1016/j.apsusc.2019.143876
12. K. Yang, B. Li, G. Zeng, Effects of temperature on properties of ZnS thin films deposited by pulsed laser deposition. Superlattices Microstruct. **130**, 409–415 (2019). https://doi.org/10.1016/j.spmi.2019.05.009
13. M. Sathishkumar, M. Saroja, M. Venkatachalam, Influence of (Cu, Al) doping concentration on the structural, optical and antimicrobial activity of ZnS thin films prepared by Sol-Gel dip coating techniques. Optik (Stuttg) **182**, 774–785 (2019). https://doi.org/10.1016/j.ijleo.2019.02.014
14. K.C. Kumar, S. Kaleemulla, Effect of Ni incorporation on structural, optical and magnetic properties of electron beam evaporated ZnS thin films. J. Phys. Chem. Solids **135**, 109028 (2019). https://doi.org/10.1016/j.jpcs.2019.05.025
15. A.M. Al-Diabat, N.M. Ahmed, M.R. Hashim, M.A. Almessiere, Growth of ZnS thin films using chemical spray pyrolysis technique. Mater. Today Proc. **17**, 912–920 (2019). https://doi.org/10.1016/j.matpr.2019.06.390
16. M. Shobana, S.R. Meher, Effect of cobalt doping on the structural, optical and magnetic properties of sol-gel derived ZnS nanocrystalline thin films and ab initio studies. Thin Solid Films **683**, 97–110 (2019). https://doi.org/10.1016/j.tsf.2019.05.037
17. S.M. Mosavi, H. Kafashan, Physical properties of Cd-doped ZnS thin films. Superlattices Microstruct. **126**, 139–149 (2019). https://doi.org/10.1016/j.spmi.2018.12.002
18. A. Jafari-Rad, H. Kafashan, Preparation and characterization of electrochemically deposited nanostructured Ti-doped ZnS thin films. Ceram. Int. **45**(17), 21413–21422 (2019). https://doi.org/10.1016/j.ceramint.2019.07.130
19. A.J. Jebathew, M. Karunakaran, K.D. Kumar, S. Valanarasu, V. Ganesh, M. Shkir, I.S. Yahi, H.Y. Zahran, A. Kathalingam, An effect of Gd3+ doping on core properties of ZnS thin films prepared by nebulizer spray pyrolysis (NSP) method. Phys. B Condens. Matter. **574**, 411674 (2019). https://doi.org/10.1016/j.physb.2019.411674
20. A. Axelevitch, B. Apter, Preparation and study of doped ZnS thin films. Microelectron. Eng. **170**, 39–43 (2017). https://doi.org/10.1016/j.mee.2016.12.027
21. F.M. Mwema, E.T. Akinlabi, O.P. Oladijo, J.D. Majumdar, Effect of varying low substrate temperature on sputtered aluminium films. Mater. Res. Express **6**(5), 056404 (2019). https://doi.org/10.1088/2053-1591/ab014a
22. J.E. Greene, Review Article: tracing the recorded history of thin-film sputter deposition: from the 1800s to 2017. J. Vac. Sci. Technol. A **35**(5), 05C204 (1800s). https://doi.org/10.1116/1.4998940
23. T.K. Pathak, V. Kumar, L.P. Purohit, H.C. Swart, R.E. Kroon, Substrate dependent structural, optical and electrical properties of ZnS thin films grown by RF sputtering. Phys. E Low-Dimensional Syst. Nanostructures **84**, 530–536 (2016). https://doi.org/10.1016/j.physe.2016.06.020
24. A. Le Donne, D. Cavalcoli, R.A. Mereu, M. Perani, L. Pagani, M. Acciarri, S. Binetti, Study of the physical properties of ZnS thin films deposited by RF sputtering. Mater. Sci. Semicond. Process. **71**, 7–11 (2017). https://doi.org/10.1016/j.mssp.2017.06.042
25. F. M. Mwema, E. T. Akinlabi, O. P. Oladijo, Influence of sputtering power on surface topography , microstructure and mechanical properties of aluminum thin films, in Proc. of the Eighth Intl. Conf. on Advances in Civil, Structural and Mechanical Engineering—CSM 2019, 2019, pp. 5–9. https://doi.org/10.15224/978-1-63248-170-2-02
26. F.M. Mwema, E.T. Akinlabi, O.P. Oladijo, Two-dimensional fast fourier transform analysis of surface microstructures of thin aluminium films prepared by radio-frequency (RF) magnetron sputtering. Mater. Sci. Eng. Lect. Notes Mech. Eng. Adv. (2019). https://doi.org/10.1007/978-981-13-8297-0_27
27. R. Zhang, B. Wang, L. Wei, Influence of RF power on the structure of ZnS thin films grown by sulfurizing RF sputter deposited ZnO. Mater. Chem. Phys. **112**(2), 557–561 (2008). https://doi.org/10.1016/j.matchemphys.2008.05.089
28. J. Kim, C. Park, S.M. Pawar, A.I. Inamdar, Y. Jo, J. Han, J.P. Hong, Y.S. Park, D.Y. Kim, W. Jung, H. Kim, H. Im, Optimization of sputtered ZnS buffer for Cu_2ZnSnS_4 thin film solar cells. Thin Solid Films **566**, 88–92 (2014). https://doi.org/10.1016/j.tsf.2014.07.024
29. P. Chelvanathan, Y. Yusoff, F. Haque, M. Akhtaruzzaman, M.M. Alam, Z.A. Alothman, M.J. Rashid, K. Sopian, N. Amin, Growth and characterization of RF-sputtered ZnS thin film deposited at various substrate temperatures for photovoltaic application. Appl. Surf. Sci. **334**, 138–144 (2015). https://doi.org/10.1016/j.apsusc.2014.08.155
30. V.L. Gayou, B. Salazar-Hernandez, M.E. Constantino, E.R. Andrés, T. Díaz, R.D. Macuil, M.R. López, Structural studies of ZnS thin films grown on GaAs by RF magnetron sputtering. Vacuum **84**(10), 1191–1194 (2010). https://doi.org/10.1016/j.vacuum.2009.10.023
31. P.K. Ghosh, S. Jana, S. Nandy, K.K. Chattopadhyay, Size-dependent optical and dielectric properties of nanocrystalline ZnS thin films synthesized via rf-magnetron sputtering technique. Mater. Res. Bull. **42**(3), 505–514 (2007). https://doi.org/10.1016/j.materresbull.2006.06.019
32. Ş. Ţălu, *Micro and nanoscale characterization of three dimensional surfaces Basics and applications* (Napoca Star Publishing House, Cluj-Napoca, Romania, 2015)
33. A.G. Korpi, Ş. Ţălu, M. Bramowicz, A. Arman, S. Kulesza, B. Pszczolkowski, S. Jurečka, M. Mardani, C. Luna, P. Balashabadi, S. Rezaee, S. Gopikishan, Minkowski functional characterization and fractal analysis of surfaces of titanium nitride films. Mater. Res. Express. **6**, 086463 (2019). https://doi.org/10.1088/2053-1591/ab26be

34. Ş. Ţălu, M. Bramowicz, S. Kulesza, V. Dalouji, S. Solaymani, S. Valedbagi, Fractal features of carbon–nickel composite thin films. Microsc. Res. Tech. **79**(12), 1208–1213 (2016). https://doi.org/10.1002/jemt.22779
35. R. Shakoury, S. Rezaee, F. Mwema, C. Luna, K. Ghosh, S. Jurečka, Ş. Ţălu, A. Arman, A.G. Korpi, Multifractal and optical bandgap characterization of Ta_2O_5 thin films deposited by electron gun method. Opt. Quantum Electron. **52**, 95 (2020). https://doi.org/10.1007/s11082-019-2173-5
36. Ş. Ţălu, S. Stach, A. Mendez, G. Trejo, M. Talu, Multifractal characterization of nanostructure surfaces of electrodeposited Ni-P coatings. J. Electrochem. Soc. **161**, D44–D47 (2013). https://doi.org/10.1149/2.039401jes
37. Ş. Ţălu, I.A. Morozov, R.P. Yadav, Multifractal analysis of sputtered indium tin oxide thin film surfaces. Appl. Surf. Sci. **484**, 892–898 (2019). https://doi.org/10.1016/j.apsusc.2019.04.170
38. X.T. Yin, W.D. Zhou, J. Li, Q. Wang, F.Y. Wu, D. Dastan, D. Wang, H. Garmestani, X.M. Wang, S. Talu, A highly sensitivity and selectivity Pt-SnO_2 nanoparticles for sensing applications at extremely low level hydrogen gas detection. J. Alloys Compounds **805**, 229–236 (2019). https://doi.org/10.1016/j.jallcom.2019.07.081
39. S. Stach, D. Dallaeva, Ş. Ţălu, P. Kaspar, P. Tománek, S. Giovanzana, L. Grmela, Morphological features in aluminum nitride epilayers prepared by magnetron sputtering. Mater. Sci. **33**, 175–184 (2015). https://doi.org/10.1515/msp-2015-0036
40. Ş. Ţălu, S. Stach, S. Valedbagi, S.M. Elahi, R. Bavadi, Surface morphology of titanium nitride thin films synthesised by DC reactive magnetron sputtering. Mater. Sci. **33**(1), 137–143 (2015). https://doi.org/10.1515/msp-2015-0010
41. D. Dastan, Effect of preparation methods on the properties of titania nanoparticles: solvothermal versus sol-gel. Appl. Phys. A **123**(699), 1–13 (2017). https://doi.org/10.1007/s00339-017-1309-3
42. F.M. Mwema, E. Akinlabi, P. Oladijo, The use of power spectrum density for surface characterization of thin films. Photoenergy Thin Film Mater. (2019). https://doi.org/10.1002/9781119580546.ch9
43. D. Sobola, Ş. Ţălu, S. Solaymani, L. Grmela, Influence of scanning rate on quality of AFM image: study of surface statistical metrics. Microsc. Res. Tech. **80**(12), 1328–1336 (2017). https://doi.org/10.1002/jemt.22945
44. X. Tao Yin, D. Dastan, F. Yu Wu, J. Li, Facile synthesis of SnO_2/$LaFeO_3$-XNX composite: photocatalytic activity and gas sensing performance. Nanomaterials (Basel, Switzerland) **9**(8), 1163 (2019). https://doi.org/10.3390/nano9081163
45. R. Swanepoel, Determination of the thickness and optical constants of amorphous silicon. J. Phys. E **16**(12), 1214–1221 (1983). https://doi.org/10.1088/0022-3735/16/12/023
46. A.G. Korpi, S. Rezaee, C. Luna, Ş. Ţălu, A. Arman, A. Ahmadpourian, Influence of the oxygen partial pressure on the growth and optical properties of RF-sputtered anatase TiO2 thin films. Results in physics **7**, 3349–3352 (2017). https://doi.org/10.1016/j.rinp.2017.08.018
47. C. Luna, A.D. Cuan-Guerra, E.D. Barriga-Castro, N.O. Núñez, R. Mendoza-Reséndez, R., Confinement and surface effects on the physical properties of rhombohedral-shape hematite (α-Fe2O3) nanocrystals. Mater. Res. Bull. **80**, 44–52 (2016). https://doi.org/10.1016/j.materresbull.2016.03.029
48. Mountains Map® 8 premium Software (Digital Surf, Besançon, France). https://www.digitalsurf.fr. Accessed 26 Oct 2019

Publisher's Note Springer Nature remains neutral with regard to jurisdictional claims in published maps and institutional affiliations.